

Examination of green roofs' cooling effects in a big city based on multi-source remote sensing data: An example from central Xi'an, China



Xiya Yan^{a,b}, Jianhong Liu^{a,b,c,*}, Wei Zhang^{a,b}, Ziqi Wang^{a,b}, Ruolan Jia^{a,b}, Lei Wang^{a,b}, Nan Liu^{a,b}, Yu Zhu^d

^a Shaanxi Key Laboratory of Earth Surface System and Environmental Carrying Capacity, College of Urban and Environmental Sciences, Northwest University, Xi'an 710127, PR China

^b Shaanxi Key Laboratory of Carbon Neutral Technology, Northwest University, Xi'an 710127, PR China

^c Shaanxi Xi'an Urban Ecosystem National Observation and Research Station, National Forestry and Grassland Administration, Xi'an 710127, PR China

^d Zhejiang University Urban-Rural Planning & Design Institute Co. Ltd., Hangzhou 310000, PR China

ARTICLE INFO

Keywords:

Green roofs
Cooling effect
Bare roofs
LST downscaling
Inter-year comparison
Intra-year comparison
Central Xi'an

ABSTRACT

As land resources for large-scale green space are limited, green roofs are crucial for urban greening and mitigating the urban heat island effect. Although studies have explored the cooling effects of green roofs, they primarily focus on meso- to micro-scale analyses, lacking a comprehensive understanding at the urban scale. This study used multi-source remote sensing data to assess the cooling effects of green roofs in a large northwestern Chinese city. Two types of green roofs were defined: Type I (bare in 2019, green in 2022) and Type II (existing green roofs in 2024), as identified through Google Earth imagery. The 30-meter Landsat-8 land surface temperature data were downscaled to a 10-meter resolution. Then we performed inter-year comparisons to assess cooling effects associated with Type I green roofs, while intra-year comparisons examined the cooling effects of Type II green roofs versus surrounding bare roofs. Afterwards, machine learning based approach was adopted to assessing the dominant factors governing green roof cooling efficacy. Results indicate that greening building roofs can reduce city-level temperatures by 0.47 °C based on inter-year comparisons. Intra-year comparisons reveal an average air temperature reduction of 2.49 °C compared to surrounding bare roofs. The Local Climate Zone (LCZ) classification emerged as the dominant predictor of green roof cooling efficacy, and concurrent enhancements in surrounding blue infrastructure and vegetation amplified cooling performance, while increased built-up density exhibited thermal interference, demonstrating context-dependent optimization strategy for urban heat mitigation.

1. Introduction

Driven by coupled global climate change and urbanization, cities worldwide are experiencing increasingly severe warming (Liu et al., 2022; Gao et al., 2024), particularly during summer months. The proliferation of impervious, heat-absorbing surface coupled with declining urban green-blue infrastructure has exacerbated anthropogenic thermal anomalies, manifesting as intensified urban heat island (UHI) effect (Devadas et al., 2009). For example, a nation-wide analysis of 302 Chinese cities revealed that mid-latitude megacities exhibit pronounced UHI intensity (Yang et al., 2019). The escalating thermal stress in cities poses multifaceted threats, including heightened public health vulnerability (Wang et al., 2025), surges in energy use (Wang et al., 2023),

disruptions to food systems (Kroeger, 2023), and deterioration of urban air quality (Cichowicz and Bochenek, 2024).

Green and blue space is an effective means to alleviate urban heat phenomena (Gunawardena et al., 2017). Extensive research has demonstrated that urban green spaces serve as effective mitigators of summer heated-induced thermal phenomena (Zhang et al., 2024; Degefu et al., 2023; Tan et al., 2021). However, current urban population surge and rapid expansion of impervious surfaces during urbanization process have led to substantial depletion of urban green infrastructure (Liu et al., 2025). Given that land resources are severely constraint in big cities, building roofs constitute underutilized spatial spaces with significant potential for conversion into extensive green zones capable of exerting positive impacts on urban thermal

* Corresponding author.

E-mail address: jhliu@nwu.edu.cn (J. Liu).

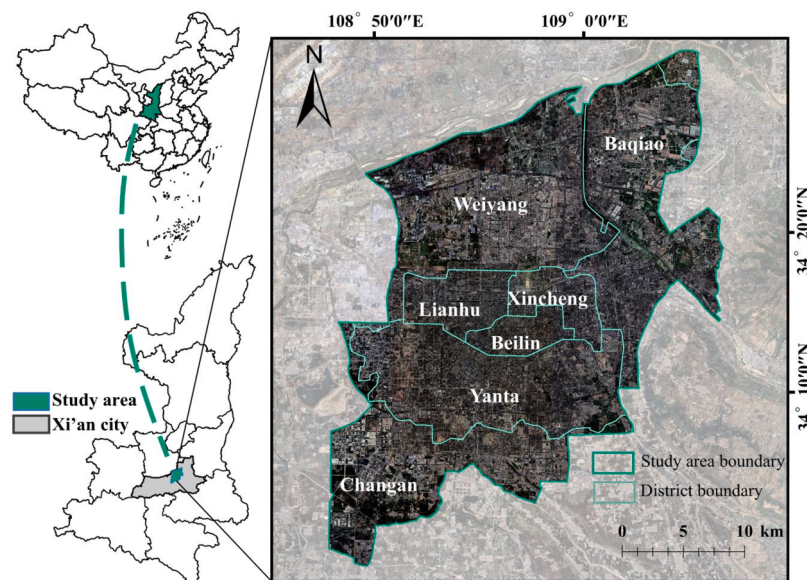


Fig. 1. Location of the study area.

environment (Jahangir et al., 2024). This context has positioned green roof systems as a critical urban planning intervention for augmenting urban green space coverage.

Empirical studies have consistently demonstrated that vegetated roof systems attenuate heat storage and thermal exchange within the near-surface atmosphere through synergistic mechanisms of plant transpiration coupled with substrate-mediated moisture evaporation (Kumar et al., 2016). These systems enhance evapotranspiration rates from roof surfaces while simultaneously suppressing sensible heat flux transfer to the urban ambient environment (Schmitz et al., 2018). When compared to conventional roof systems, green roofs demonstrate superior capacity in transforming incident energy into latent heat flux through vegetation processes, as evidenced by multiple experimental investigations (Tan et al., 2022; Sailor et al., 2014; Li et al., 2014). This thermoregulatory mechanism establishes green roof implementation as an urban climate adaption strategy for thermal load mitigation in built environment (Sharma et al., 2016; He et al., 2020).

The thermal regulation capacity of green roofing systems has been extensively quantified in urban climatology research. Although green roofs may exhibit a temporary warming effect during the day, they provide significant cooling benefits during the summer months (Zheng et al., 2021). Site-specific empirical investigations revealed a proportional relationship between green roof coverage and thermal mitigation efficacy. For example, research conducted in Melbourne, Australia, demonstrated that increasing green roof coverage from 30 % to 90 % could reduce the maximum daytime roof surface temperature by 1 °C to 3.8 °C (Imran et al., 2018). Similarly, a study conducted in downtown Austin, Texas, found that converting 4.2 % of the total rooftop area to green roofs resulted in an average reduction of 2.80°F in the daytime land surface urban heat island (Kafy et al., 2024). By integrating a micro-level computational fluid dynamics model and a building energy simulation method to assessing the cooling effects of green roofs across 43 megacities around the world, Jia et al. (2025) demonstrated that installing green roofs can achieve a maximum cooling effect of up to 0.8 °C in urban areas. This finding is supported by cross-city and cross-climate simulation analyses, highlighting the significant role of green roofs in mitigating the urban heat island effect.

However, current scientific research into the thermal mitigation performance of green roofs has been predominantly confined to meso-micro scale analyses (Berardi, 2016; Jamei et al., 2023; Zheng et al., 2023), thereby constraining our comprehension of their city-scale climatic interactions. This research gap hinders a comprehensive

understanding of the cooling potential of green roofs across the entire city, highlighting the urgent need for city-scale studies. Investigations exploring the cooling effects of green roofs at the urban scale have utilized INVEST model (Zhuang et al., 2021; Jahangir et al., 2024) and numerical weather prediction models (Georgescu et al., 2013; Kim et al., 2025; Wang et al., 2022). However, these models necessitate complex parameterization schemes and multi-source datasets, including meteorological, urban canopy characteristics, green roof vegetation attributes, and hydrological data. The requisite data processing and model calibration procedures present significant challenges for urban planning practitioners lacking specialized computational resources and domain-specific expertise. Consequently, there is a pressing need for novel methodological frameworks capable of simulating large-area urban thermal environmental optimization through green roof implementation.

Satellite remote sensing is a vital means for acquiring the multi-source data necessary to evaluate the cooling effects of green roofs on a large scale (Phelan et al., 2015), including the distribution of urban green infrastructure, thermal infrared-derived land surface temperature (LST), 3D building morphology parameters, and soil or vegetation water content. Information regarding green vegetation is particularly crucial because the thermoregulatory capacity of green roofs is principally mediated through phytogenic processes including foliar transpiration and canopy radiative shielding. Advanced remote sensing technology shows great capacity in mapping vegetation coverage, retrieving plant biophysical parameters, and vegetation structure, which yields mechanistic insights into the microclimate modulation potential of inherent in vegetated roofing systems.

LST is a critical geographical parameter for assessing the cooling effect of green infrastructure. Satellite-based thermal remote sensing technology enables the acquisition of spatiotemporally continuous thermal data with high spatial resolution, which is essential for investigating the cooling effects of green roofs at an urban scale (Lin et al., 2021). For example, Herrera-Gomez et al. (2017) examined green roofs' climate change mitigation potential in Serbia and Spain using Landsat 7 ETM+ and Sentinel-2 images, and found that thermal effects could be mitigated when the roof greening coverage reached 40.6 %. Similarly, Dong et al. (2020) used land surface temperature inversion technology and Landsat-8 imagery to quantitatively evaluate the cooling effect of green roofs on Xiamen Island, China, which effectively reduced the temperature by 0.91 °C.

To investigate the cooling effects of urban green roofs, higher spatial

resolution thermal datasets are necessary to analyze microscale thermal variance across built environment components (Dominguez et al., 2011). Spatially derived high-resolution LST measurements can accurately reflect the extent of surface temperature reduction achieved by green roofs. The temperature regulation effects of green vegetation can be quantified by comparing the temperature differences between green and bare roofs. However, current satellite-based solutions exhibit distinct technical tradeoffs: Landsat-8's thermal infrared sensor (TIRS) provides 100-m LST data with open-access policy for urban climatology investigations, whereas Sentinel-2's multi-spectral instrument (MSI) delivers 10-meter resolution multi-spectral imagery but thermal band absence constricts its direct application in urban thermal studies (Chaves et al., 2020). To address this resolution gap, Katarína et al. (2022) took advantage of the known relationship between LST and land cover indicators and used Sentinel-2 equivalent spectral data to define a spectral index based on Landsat8 data and an LST multivariate linear regression model to downscale LST to 10 m resolution.

To bridge this critical research gap, this study presents a comprehensive assessment of the urban-scale thermal mitigation performance of green roofs by synergistically integrating multi-platform remote sensing data (Landsat-8, Sentinel-2, and high-resolution Google Earth imagery) with advanced GIS spatial analysis techniques. The specific objectives are as follows:

- (1) An inter-year comparison to assess whether green roofs have a cooling effect by analyzing the LST of the same roofs before (in 2019) and after (in 2022) greening.
- (2) An intra-year comparison to illustrate the magnitude of the cooling effects by comparing the average LST of green roofs and their neighboring bare roofs in the summer of 2024.
- (3) A machine learning based approach to detect the determinants governing green roof's cooling efficacy.

2. Materials and methods

2.1. Study area

The study area comprises the central urban zone of Xi'an City, Shaanxi Province, China (Fig. 1), geographically located between 34°27'N-34°30'N latitude 108°47'E-109°7'E longitude. This administrative region spans seven municipal districts: Weiyang, Baqiao, Lianhu, Xincheng, Beilin, Yanta, and Chang'an, encompassing a total land area of 766 km².

Xi'an is situated on the Guanzhong Plain, featuring relatively low-lying topography bounded by the Qinling Mountains to the south and the Weihei Plateau to the north. This unique geomorphological configuration results in constrained atmospheric circulation and pronounced heat retention characteristics. The city experiences a semi-humid warm-temperate continental monsoon climate with four distinct seasons. Summer months are typically hot and pluvial, with a recorded average air temperature of 27.7 °C, an average relative humidity of 59 %, and an average wind velocity of 1.6 m/s (China Statistical Yearbook, 2018). Annual precipitation in Xi'an is approximately 571 mm based on recent meteorological records (Xi'an Statistical Yearbook, 2023). In contrast to comparable semi-humid climate cities like Jinan (elevated summer humidity) and Zhengzhou (stronger monsoon influence)—both situated in well-ventilated plains/hill regions with homogeneous thermal distribution—Xi'an's inland northwestern allocation contributes to its distinctive aridity (Zhou et al., 2017; Liu et al., 2009).

Xi'an has experienced rapid urbanization in recent decades, with significant increases in urban construction land and a rapidly growing population (Liang et al., 2021). Liu et al. (2023) conducted a comprehensive ecological quality assessment of Xi'an's metropolitan area, and showed that urban ecological quality declined during 2000–2019 owing to multiple natural and anthropogenic factors. The synergistic interaction of topographic constraints, climatic patterns, and urban expansion

mechanisms has established thermal vulnerability patterns, manifesting in prolonged summer heat extremes. Historical meteorological records revealed a 14-day continuous heatwave event in 2018 (Yuan et al., 2022). A notable heat event in 2017 caused many heat-related illnesses and infrastructure failures across municipal power grids (Qu et al., 2018). In June 2022, the city experienced an unprecedented 72-hour thermal anomaly with temperatures surpassing 40 °C (Shaanxi Meteorological Administration).

As of 2020, Xi'an operationalized 149 municipal parks comprising 4803 ha dedicated parkland and 36,034 ha of integrated green infrastructure, collectively achieving a 41.54 % green coverage rate in urbanized areas. However, spatial analysis reveals the distribution of green space within the study area is uneven. As of 2018, vegetated roof systems occupied 800,000 m², accounting for 0.73 % of the total roof area (Guan, 2019).

2.2. Data sources and processing

This study utilized multi-source remote sensing data, including Google Earth, Sentinel-2A multi-spectral imaging (MSI), and Landsat-8 thermal infrared sensor (TIRS) images. All the selected images were high-quality and exhibited no cloud coverage or missing values within the study area. Detailed information on each data source is provided below.

2.2.1. Google Earth images

High-resolution images obtained from Google Earth were used to extract the green roofs manually in this study. They were acquired in July 2019, August 2022, and August 2024. These images were already geo-referenced and had a resolution of 0.597 m. They were used to extract the green roofs manually.

2.2.2. Sentinel-2A MSI images

Sentinel-2A MSI images were acquired on July 28, 2019, August 6, 2022, and July 25, 2024 (European Space Agency, ESA, <https://dataspace.copernicus.eu>). These images exhibited less than 10 % cloud cover, with clouds primarily concentrated near the surrounding mountains and absent in the study area. The downloaded imagery has been geometrically corrected.

The Sentinel-2A MSI images served a dual purpose in this study. First, they were utilized to calculate the Normalized Difference Vegetation Index (NDVI) values of the extracted green roofs, enabling the exclusion of pseudo-green roofs identified from Google Earth imagery. Second, they facilitated the calculation of three land cover indices, i.e. NDVI, Normalized Difference Building Index (NDBI), and Normalized Difference Water Index (NDWI), to estimate the LST at a 10-meter resolution.

2.2.3. Landsat-8 OLI/TIRS images

Landsat-8 Operational Land Imager (OLI) and TIRS images were acquired on July 28, 2019, August 5, 2022, and July 25, 2024, at 3:33 AM (United States Geological Survey, USGS, <http://glovis.usgs.gov/>). The cloud cover percentages for these scenes were 10.49 %, 8.09 %, and 7.86 %, with no cloud cover in the study area. The Landsat-8 OLI/TIRS sensor comprises 11 bands, 9 in the visible and near-infrared spectrum (B1-B9) and 2 in the thermal infrared region (B10-B11). The OLI imagery included 8 reflective bands (B1-B7, B9) with an original spatial resolution of 30 m, whereas the panchromatic band (B8) had a resolution of 15 m. The thermal bands (B10-B11) originally had a spatial resolution of 100 m but were resampled to 30 m by the USGS (<https://earthexplorer.usgs.gov/>). As the same, the downloaded Landsat-8 images have also been geometrically corrected.

This study used Landsat-8 TIRS imagery to compute the LST, whereas OLI imagery was employed to calculate the three land cover indices.

The integration of multi-source satellite imagery with varying spatial resolutions introduced significant technical challenges in data

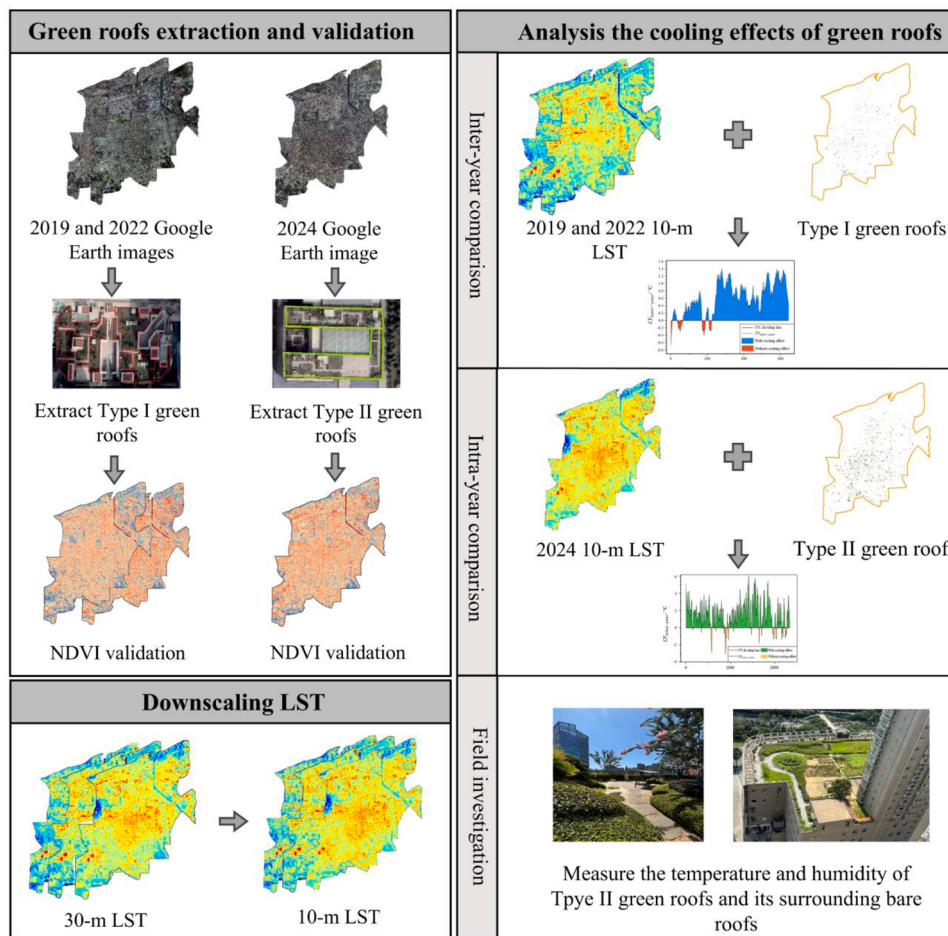


Fig. 2. Flowchart of the methodology used in this study.

harmonization and comparative analysis. To ensure data consistency and interoperability, the following steps were adopted:

- (1) Radiometric calibration and atmospheric correction were systematically applied to both Landsat-8 and Sentinel-2 datasets to eliminate sensor-specific radiometric biases and atmospheric interference effects.
- (2) All geospatial datasets (including auxiliary Google Earth imagery) were standardized to a common coordinate reference system (WGS84 UTM Zone 49 N) through rigorous projection transformation to ensure geometric consistency.
- (3) Bilinear resampling of Landsat-8 datasets to 10-meter resolution to facilitate LST downscaling later.

2.2.4. Building vectors

Building vectors within the study area in 2024 were obtained from Resource and Environmental Science Data Platform (<http://www.igsnrr.ac.cn/>), which is supported by the Institute of Geographic Sciences and Resources of the Chinese Academy of Sciences. The georeferenced building vector dataset encodes vertical elevation attributes through standardized floor-count quantification. However, not all building vectors are aligned with the building top boundaries on the Google Earth imagery. Therefore, these building vectors manually adjusted to make sure their boundaries were aligned with the building top boundaries on the Google Earth imagery. The adjusted building roof vectors are the base of green roofs extraction and the cooling effect analysis.

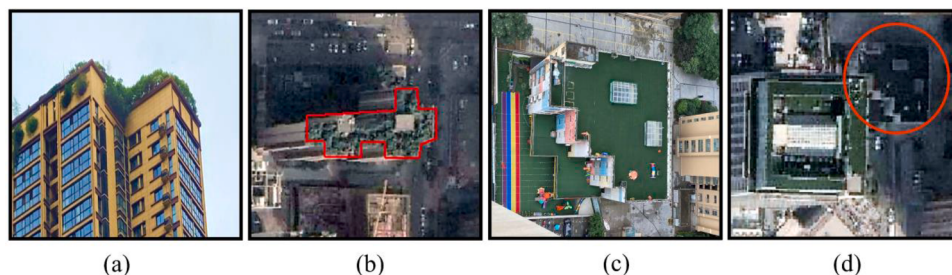


Fig. 3. Examples of real and pseudo green roofs in the study area. (a) is a real green roof, and (c) is a pseudo green roof. (a) and (c) are photos taken on site, and (b) and (d) are their corresponding Google Earth imagery.

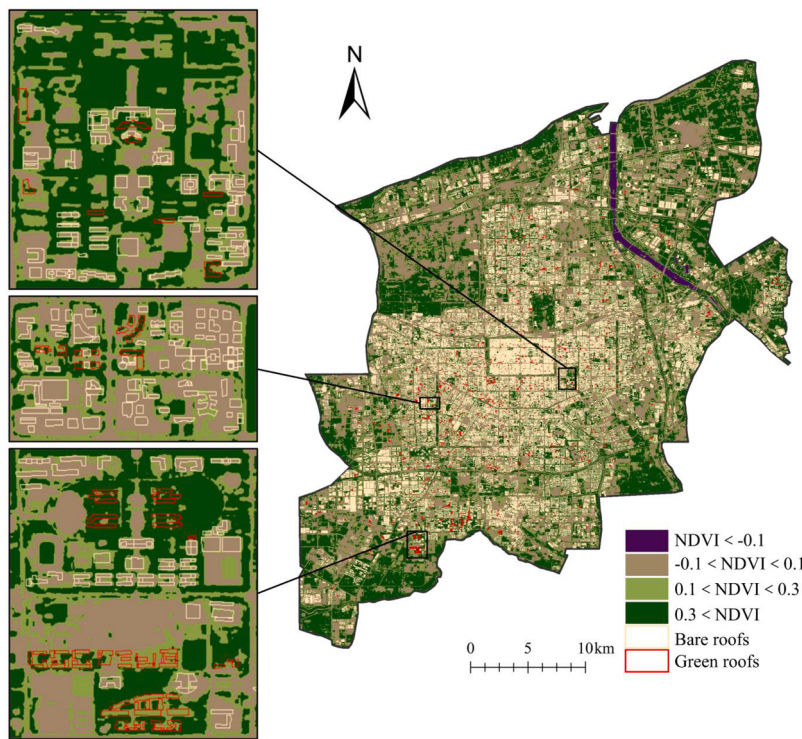


Fig. 4. NDVI map with three examples for zoom-in display for the year 2024. It shows that bare roofs located in yellow-brown regions, while green roofs are in green regions.

2.3. Research methodology

2.3.1. Flowchart of the technique

Fig. 2 illustrates the methodological flowchart employed in this study, which comprises five key steps. In the first step, two distinct types of green roofs (Type I and Type II) were identified based on visual interpretations of Google Earth imagery. The NDVI was calculated to accurately identify authentic green roofs while excluding areas that exhibited characteristics of pseudo-green roofs. In the second step, the 30-meter LST data were downscaled to a 10-meter resolution using linear regression and convolution residual methods. Subsequently, an inter-year comparison was conducted to assess whether there was a cooling effect after the greening of roofs based on Type I green roofs. In the fourth step, an intra-year comparison was performed to delineate the extent of cooling effects associated with Type II green roofs. Finally, temperature and humidity measurements of both the bare and green roofs were obtained during a field investigation conducted in summer 2024.

2.3.2. Green roof extraction and validation

Before the manual identification process, an analysis of authentic green and pseudo-green roofs' distinguishing features was conducted through field investigation. Authentic green roofs are characterized by the presence of vegetation, including grasses, shrubs, and trees, resulting in a coarse texture in high-resolution images accompanied by noticeable variations in brightness owing to the uneven canopies of shrubs and trees (Figs. 3(a)–(b)). In contrast, pseudo-green roofs, which are typically covered with artificial materials such as synthetic grass, exhibit a uniform appearance in high-resolution images, characterized by a smooth texture and little to no variation in brightness (Figs. 3(c)–(d)).

Then the visual interpretation and manual digitization were performed on ArcGIS 10.6 platform. Due to the large size of the study area, we first divided it into different subzones according to the administrative subdistricts to prevent missed screening targets. Then ever building roof in each subzone was screened based on Google Earth imagery. If the

roof is fully vegetated, it was labeled as a green roof, otherwise if it is partially vegetated, then we digitized the boundary of the green covered roof area.

Despite careful attention paid to the extraction of green roofs, some misinterpretations may still occur. We employed the NDVI to validate the digitized green roof vectors to address this issue. The NDVI was calculated using reflectance values from the red and near-infrared bands (see Eq. (1)) and serves as an indicator of vegetation growth (Huete et al., 2002; Pettorelli et al., 2005). The NDVI values range from −1 to 1, where values approaching 1 indicate high-density vegetation or periods of vigorous growth (Reed et al., 1994). Conversely, values near zero suggest the presence of bare ground or soil, whereas values less than zero represent non-vegetative surfaces, such as water bodies.

$$NDVI = \frac{NIR - RED}{NIR + RED} \quad (1)$$

Where NIR is the near-infrared band (band 8) of the Sentinel-2A MSI images and RED is the red band (band 4).

Fig. 4 delineates the NDVI characteristics of bare versus vegetated roof surfaces. A clear distinction emerges between the two categories, with bare roofs exhibiting minimal NDVI values (−0.1 to 0.1) in contrast to vegetated roofs demonstrating substantially elevated indices (>0.1), including notable instances exceeding 0.3. This dichotomy arises from the photosynthetic activity inherent to authentic vegetation-covered green roofs, which manifests characteristically strong near-infrared reflectance captured by NDVI quantification. Conversely, non-photosynthetic surfaces such as bare substrates or artificial green cladding materials lack this spectral signature, resulting in depressed NDVI measurements. Consequently, all roof surfaces with mean NDVI values below 0.1 were systematically excluded from the green roof datasets.

To validate the classification methodology, a stratified random sampling protocol selected 150 vegetated roofs annually for visual confirmation. The validation process yielded accuracy rates of 99 % (2019), 100 % (2022), and 99 % (2024), with misclassifications predominantly occurring in composite roof structures containing both

Table 1

Calculation of the three land cover indices.

Indices	Formulas	Landsat 8 bands used	Sentinel-2 band used
Normalized Difference Vegetation Index (NDVI)	(NIR-Red)/(NIR+Red)	(B5-B4)/(B5+B4)	(B8-B4)/(B8+B4)
Normalized Difference Built-up Index (NDBI)	(SWIR-NIR)/(SWIR+NIR)	(B6-B5)/(B6+B5)	(B11+B8)
Normalized Difference Water Index (NDWI)	(Green-NIR)/(Green+NIR)	(B3-B5)/(B3+B5)	(B3+B8)

biological vegetation and synthetic green materials.

Ultimately, two types of green roofs were extracted for this study: (1) roofs that were bare in 2019 but transformed into green roofs by 2022 (Type I green roofs), and (2) all green roofs present in the study area as of 2024 (Type II green roofs). A total of 645 Type I green roofs were identified distributed on 447 building tops as, and a total of 2335 Type II green roofs were identified on 1322 building tops.

2.3.3. LST downscaling

Many studies adopted the TsHARP algorithm for LST downscaling (Li et al., 2023; Kustas et al., 2003), which relies on the NDVI-LST relationship. However, urban environments are characterized by significant land cover heterogeneity and NDVI alone is insufficient to fully characterize LST variations across the entire study area. While scholars have explored machine learning techniques such as Random Forest (RF) and Support Vector Machine (SVM) that demonstrate robust nonlinear fitting capabilities, these approaches exhibit limitations including heavy reliance on extensive datasets and inadequate spatial detail reconstruction (Zhu et al., 2021; Keramitsoglou et al., 2013). In addition, although deep learning methods like Land Surface Temperature Downscaling Residual Network (LSTDNR) are proficient in handling complex nonlinear relationships with automated capacity of feature extraction and multi-source data integration, they present challenges including substantial training data requirements, computational complexity, and limited model interpretability (Zhang et al., 2021). Therefore, we adopted the linear regression model with convolution residual methodology developed by Katarína et al. (2022) for LST downscaling, which has demonstrated efficacy in urban heat island characterization through multi-sensor fusion techniques. This hybrid approach leverages 3 land cover metrics (NDVI, NDBI, and NDWI) to synergistically combine the interpretability advantages of linear models with the spatial feature capture capabilities of residual networks. Empirical validation conducted by the author involved deploying ground-based thermal infrared radiometers across heterogeneous urban typologies (e.g., vegetated parks, impervious commercial zones) to acquire 10-meter resolution reference LST datasets. The deviation of the observed data from the downscaled results is -1.55°C . The methodology is applied in many urban studies such as low carbon green urban design, environmental and ecological research (Nirwana et al., 2024; Srivastava et al., 2022).

The procedural framework consists of three stages.

2.3.3.1. Land cover index calculation. The land cover index effectively quantified the complex heterogeneous characteristics of urban environments (Bonafoni et al., 2015). The three indices (NDVI, NDBI, and NDWI) were computed using the Landsat-8 OLI red, green, near-infrared, and short infrared bands, as well as the Sentinel-2A MSI 10-m spatial resolution red, green, near-infrared, and 20 m spatial resolution short infrared bands (resampled to 10 m). The calculation formulae are listed in Table 1. Land-cover indices effectively encapsulate urban areas' complex and heterogeneous characteristics (Bonafoni et al., 2015). The 3 indices (NDVI, NDBI, and NDWI) were computed using data from Landsat 8 OLI, which has a spatial resolution of 30 m, and Sentinel-2A MSI, which offers a spatial resolution of 10 m for the red, green, and near-infrared bands and a spatial resolution of 20 m for

the short-wave infrared bands (resampled to 10 m). The mathematical formulations for these indices are listed in Table 1.

2.3.3.2. Calculation of the 30-m LST based on Landsat-8 TIRS images.

The radiative transfer equation method was used to compute the 30-m LST, as shown in Eq. (2):

$$L_{(sens,\lambda)} = [\varepsilon_\lambda B_\lambda(T_s) + (1 - \varepsilon_\lambda)L_d]\tau_\lambda + L_u \quad (2)$$

Where $L_{(sens,\lambda)}$ is the thermal radiance band of Landsat-8 TIRS (B10) ($\text{W.m}^{-2}.\text{sr}^{-1}.\mu\text{m}^{-1}$), ε_λ is the surface emissivity, $B_\lambda(T_s)$ is Planck's law/blackbody radiation ($\text{W.m}^{-2}.\text{sr}^{-1}.\mu\text{m}^{-1}$), (T_s) is the actual LST (K), L_d is the atmospheric downward radiance, τ_λ is the total atmospheric transmittance of thermal infrared radiation recorded by band 10, and L_u is the atmospheric upward radiance. Atmospheric correction parameters were calculated using the method described by Barsi et al. (2005).

2.3.3.3. Defining the LST-land cover indices model. A linear relationship was established between the three land cover indices (NDVI, NDBI, and NDWI) of Landsat-8 and the calculated LST, with LST serving as the predictor variable. All the input raster layers were maintained at a resolution of 30 m. The output coefficients (a_0-a_3) were employed to derive the LST computation metrics for Landsat-8 (Eq. (3)). These metrics were calculated using ArcMap 10.6, specifically through the Map Algebra-Raster Calculator, to obtain the LST at the 30-meter resolution.

$$LST_{30m} = a_0 + a_1 \times NDVI_{30m} + a_2 \times NDBI_{30m} + a_3 \times NDWI_{30m} \quad (3)$$

The model was subsequently applied to predict LST at a 10-meter resolution, whereby the land cover indices derived from Landsat-8 were substituted with their corresponding land cover indices from Sentinel-2A (Eq. (4)).

$$LST_{10m} = a_0 + a_1 \times NDVI_{10m} + a_2 \times NDBI_{10m} + a_3 \times NDWI_{10m} + \Delta LST_{10m} \quad (4)$$

The regression residuals were computed by subtracting the observed LST (LST_{obs}) at a 30-meter resolution from the modelled LST (LST_{30m}) (Eq. (5)).

$$\Delta LST_{30m} = LST_{30m} - LST_{obs} \quad (5)$$

ΔLST_{30m} is then resampled to ΔLST_{10m} as a 10 m cell-size grid by convolution with a Gaussian kernel of 30 m size in ArcMap.

2.3.4. Quantitative assessment of the cooling effects of green roofs

2.3.4.1. Inter-year comparison. An inter-year comparison was conducted to intuitively quantify the actual cooling benefits brought by the adoption of roof greening measures. This was achieved by comparing Type I green roofs' relative surface temperature (ΔT) in 2019 and 2022. ΔT was introduced in previous studies to mitigate the bias associated with the temporal discrepancies in remote sensing images (Domínguez et al., 2011; Jin, 2022). Specifically, ΔT is defined as the difference between the average surface temperature of each Type I green roof vector and the average surface temperature of the entire study area. Accordingly, the inter-year cooling effect ($CF_{inter-year}$) is defined as the difference in ΔT for the same Type I green roofs between 2019 and 2022. These calculations are detailed in Eqs. (6) and (7).

$$\Delta T = T_{mean}^g - T_{mean}^s \quad (6)$$

$$CF_{inter-year} = \Delta T_{2019} - \Delta T_{2022} \quad (7)$$

Where T_{mean}^g represents the average surface temperature of each Type I green roof vector and T_{mean}^s denotes the average surface temperature of the entire study area. When $\Delta T < 0$, it means that the roof's surface temperature is lower than the average surface temperature of the entire study area. Conversely, when $\Delta T > 0$, it signifies that the roof's surface temperature is higher than the average surface temperature of the entire

Table 2

Temperature measurement product parameters.

Name	Size(mm)/Weight(g)
Japanese Penguin 72,591 F15cm	Φ156 × 30/140
Name	Size(mm)/Weight(g)
Japanese Penguin 72591 F15cm	Φ156×30/140
	Inaccuracy
	±2 °C/±2 %
	Measuring range
	Teampreture:-30~50 °C
	Humidity:0~100%

study area. $CF_{inter-year}$ demonstrates the cooling effects of green roofs after their implementation in 2022. If $CF_{inter-year} > 0$, this indicates the presence of a cooling effect resulting from roof greening.

A paired *t*-test was conducted in the SPSS software for each Type I green roof with ΔT_{2019} and ΔT_{2022} to examine whether the same roof had a cooling effect after the implementation of greening on building roofs. When the probability of the main parameter of the paired *t*-test is $P \leq 0.01$, it is considered to be significantly different, which means there is a significant cooling effect after the implementation of green roofs.

2.3.4.2. Intra-year comparison. An intra-year comparison was conducted to reflect the ability of green roofs to regulate local thermal environments by comparing the average surface temperature of Type II green roofs with that of the surrounding bare roofs during the summer of 2024. To facilitate comparison, a buffer zone with a radius of 500 m was established around each Type II green roof (Due to the fact that the distance between road networks in Xi'an is generally between 500–800 m, a 500-meter buffer zone can cover typical block units, ensuring that the comparison samples of bare roofs and roof greening are in the same urban environment as much as possible. If expanded, additional variables will be added). Therefore, the intra-year cooling effect ($CF_{intra-year}$) is defined as the difference between the average LST of bare roofs within a 500-m buffer zone of each Type II green roof and the average LST of each Type II green roof (Eq. (8)). A $CF_{intra-year}$ value greater than zero indicates a cooling effect.

$$CF_{intra-year} = T_{mean}^b - T_{mean}^g \quad (8)$$

Where T_{mean}^b represents the mean LST of the bare roofs within the 500-m buffer zone, and T_{mean}^g is the average LST of Type II green roof.

2.3.4.3. Assessing key determinants governing green roof cooling efficacy. Existing studies have demonstrated that LST is influenced by multiple environmental determinants (Wang et al., 2022), which implies these factors may similarly govern the cooling efficacy of green roofs. The intrinsic characteristics considered are green roof area and its building height. Environmental determinants considered in this study includes vegetation cover, built environment intensity and blue infrastructure. Therefore, we calculated mean NDVI, NDBI, NDWI within 500-m buffer of each green roof.

The Local Climate Zone (LCZ) serve as a crucial framework for understanding and managing urban land use patterns, especially in relation to urban climate and the UHI. To obtain the LCZ map for our study area, we first delineated 10 distinct LCZ types based on the architectural and environmental characteristics. Then we collected training samples on Google Earth platform for each LCZ type and exported them as a KML file. Afterwards, we uploaded the KML file to the World Urban Database

and Access Portal Tools (WUDAPT) portal (<http://www.wudapt.org/>) and obtained the LCZ classification results. Finally, the initial LCZ classification outputs were further refined in ArcGIS 10.6 to ensure accuracy and spatial coherence.

Given the mixed data structure encompassing both categorical (e.g., LCZ types) and continuous variables in our experiment, the study employs an integrated Random Forest (RF) and SHapley Additive exPlanations (SHAP) approach to elucidate multi-factor interaction mechanisms. This dual approach uniquely integrates ensemble learning algorithms with cooperative game theory principles to decode multi-factorial interaction networks.

The RF algorithm demonstrates exceptional competence in processing high-dimensional feature spaces through its distinctive bootstrap aggregation (bagging) methodology and random subspace selection protocol (Breiman, 2001). By constructing an ensemble of decorrelated decision trees, it simultaneously achieves: (i) robust prevention of overfitting, (ii) automatic detection of nonlinear associations, and (iii) implicit quantification of higher-order interaction effects among disparate variable types (Liu et al., 2021). Complementarily, SHAP analysis provides mathematically rigorous decomposition of predictive outputs into marginal feature contributions, enabling precise quantification of each parameter's influence magnitude, directional impact (positive/-negative), and interaction of heterogeneous factors on cooling efficiency (Lundberg and Lee, 2017). This synergistic combination facilitates both accurate identification of dominant controlling factors and mechanistic interpretation of complex feature interdependencies.

Notwithstanding these advantages, two critical methodological constraints require acknowledgment: First, the framework's performance is contingent upon data completeness - missing values may compromise result validity, while sampling bias in training data could distort SHAP interpretation. Second, strong feature collinearity may induce allocation instability in SHAP value distributions, necessitating careful correlation diagnostics during analysis.

In this study, we first analyzed the factors influencing Type II green roofs' cooling capacity in 2024. The multi-scale predictors include intrinsic characteristics (green roof area, building height), categorical LCZ types, and surrounding environmental indices (characterized by mean NDVI, NDBI, NDWI within 500-m buffer). Since LCZ type is a categorical variable, but the explanation of SHAP values for categorical variables is usually based on their numerical encoding, which may affect the interpretability of the results. Therefore, LCZ type was included in RF analysis for identify importance of different factors, but as excluded in the SHAP value analysis. Assuming LCZ types and building heights didn't change during the 2019–2022 study period, we further assessed the impacts of changing surrounding environment (characterized by differential mean NDVI, NDBI, NDWI within 500-m buffer) and the area extent on the cooling efficacy of the newly built green roofs (Type I green roofs).

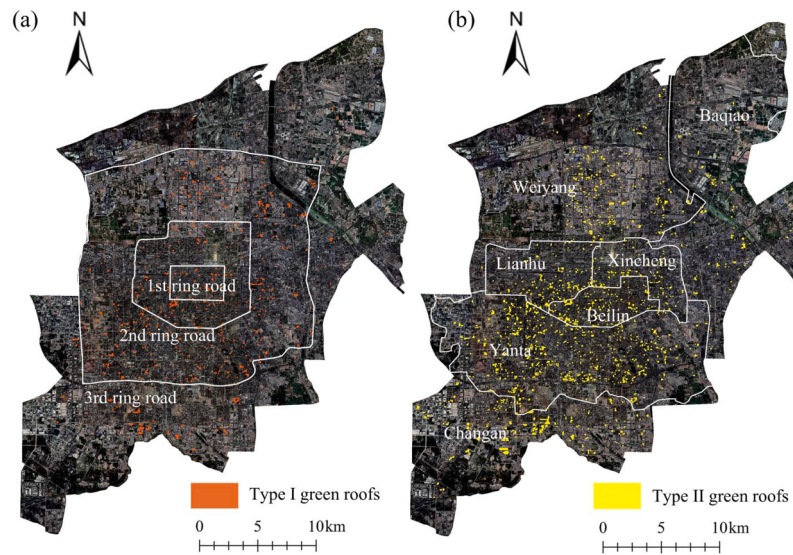


Fig. 5. The spatial distribution of type I (a) and type II (b) green roofs extracted in this study.

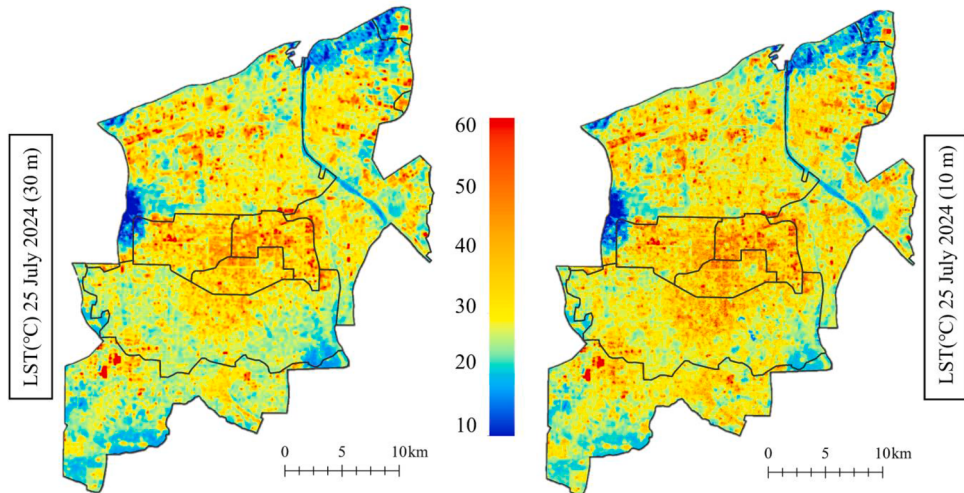


Fig. 6. The 30-m original and 10-m downscaled LST images in 2024.

2.3.4.4. Field investigation. To assess the actual effectiveness of green roofs in reducing temperature, a field investigation was conducted on sunny days between July 29, 2024, and August 31, 2024, from 11:00 to 16:00. Given access restrictions stemming from private property rights, the empirical data collection focused on publicly accessible rooftops predominantly associated with commercial facilities. To enable rigorous comparison of cooling efficacy across green roof configurations, this study incorporated a representative sample of 25 vegetated roof systems including garden type, semi-garden type and simple type were selected in this paper. The air temperature and humidity were measured at 60 cm above the roof surface using a Japanese Penguin 72,591 device. Wind direction and speed data were obtained using the Windy app. The measurement tools are listed in Table 2.

3. Results and analysis

3.1. Types of green roofs extracted

Fig. 5 shows the extracted Type I and Type II green roofs in this study. A total of 645 Type I green roofs (bare in 2019 but green in 2022) were identified, (Fig. 5(a)), which collectively covered an area of 0.28

km², with individual roof areas ranging from a minimum of 7.52 m² to a maximum of 6476.89 m², yielding an average area of 436.36 m². Type I green roofs are predominantly located within the Third Ring Road of the study area, which is highly populated, densely inhabited, and characterized by a dispersed and non-contiguous distribution. A total of 2335 Type II green roofs (all green roofs in 2024) were extracted (Fig. 5(b)). The total area of these roofs is 1.41 km², which represented 1.78 % of the total building roof area in the study region. The size of these roofs varied significantly, with the smallest measuring 3.05 m² and the largest spanning 11,874.60 m², resulting in an average area of 603.48 m². Type II green roofs were primarily concentrated in the most densely populated built-up areas of Xi'an, specifically the administrative districts of Beilin, Lianhu, Xincheng, and Yanta.

3.2. Cooling effects of the green roofs

3.2.1. The inter-year comparison

Landsat-8-derived LST on July 28, 2019, August 5, 2022, and July 25, 2024 were downsampled to 10-meter resolution. Fig. 6 presents the 30-m original and 10-m downscaled LST in 2024. Validation revealed robust agreement between the original 30-m LST and the enhanced 10-

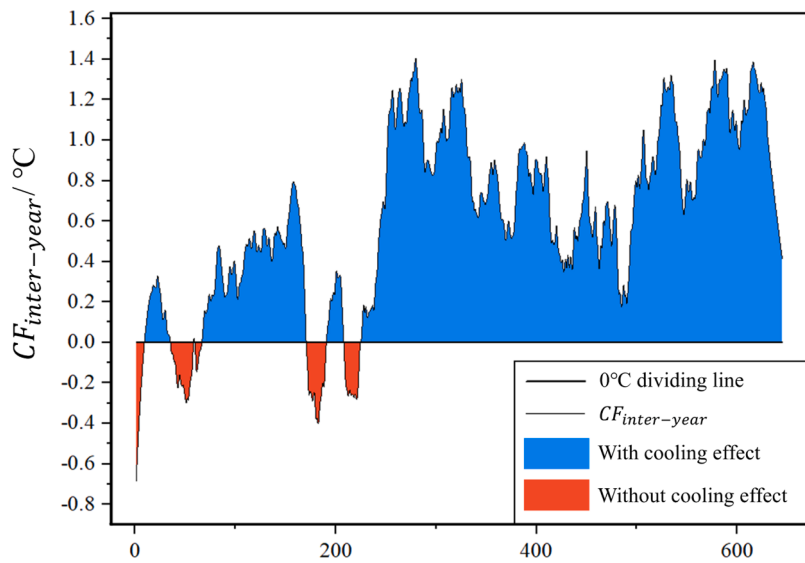


Fig. 7. The inter-year cooling effect based on type I green roofs.

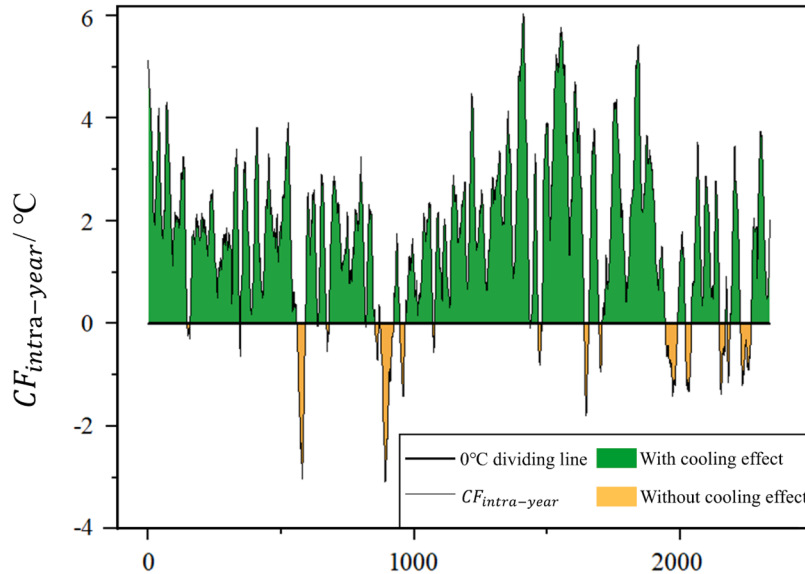


Fig. 8. The intra-year cooling effect of type II green roofs.

m datasets, with regression analyses yielding determination coefficients (R^2) of 0.83 (2019), 0.74 (2022), and 0.81 (2024). The corresponding Pearson's correlation coefficients (ρ) reached 0.91 (2019) and 0.86 (2022), exceeding the 0.80 threshold for strong linear associations. These temporal validation results demonstrate sustained precision in the thermal downscaling algorithm's performance across multi-annual observations. Therefore, further assessment of cooling effects was based on the 10-m LST datasets.

The inter-year comparison aimed to assess the cooling effects of greening roofs by comparing the difference of their surface temperatures with the regional background before and after greening. The results revealed that Type I green roofs significantly reduced urban temperatures (Fig. 7). Specifically, the study area's average temperature in 2019 was 38.56 °C, while Type I green roofs exhibited an average temperature of 39.32 °C, indicating a positive thermal differential (mean $\Delta T_{2019} = 0.76$ °C). However, post-greening monitoring in 2022 showed a reversal, with Type I green roofs demonstrating sub-ambient temperatures of 37.73 °C compared to the regional baseline of 38.02 °C, resulting in a cooling magnitude of 0.29 °C relative to 2019 conditions. This translates

to an overall temperature reduction of 0.47 °C when considering the change from pre-greening to post-greening conditions. Statistical analysis using a paired *t*-test confirmed these cooling effects to be significant ($P \leq 0.01$).

Notably, the comparative analysis described above was conducted against the regional thermal baseline (study area mean), a methodological approach that inherently yields conservative estimation outcomes. Subsequent calculations of impervious surface thermal characteristics revealed persistently elevated land surface temperature (LST) values, with mean measurements of $\mu=39.87$ °C in 2019 and $\mu=39.44$ °C in 2022. Comparative analysis demonstrated that green roof implementation achieved a 0.55 °C cooling magnitude relative to impervious surfaces, exceeding the differential observed relative to the study area mean. These findings substantiate the enhanced cooling potential discernible through targeted comparative analysis between green infrastructure and urban heat-retentive surfaces.

3.2.2. The intra-year comparison

The intra-year comparison focused on quantifying the cooling effects

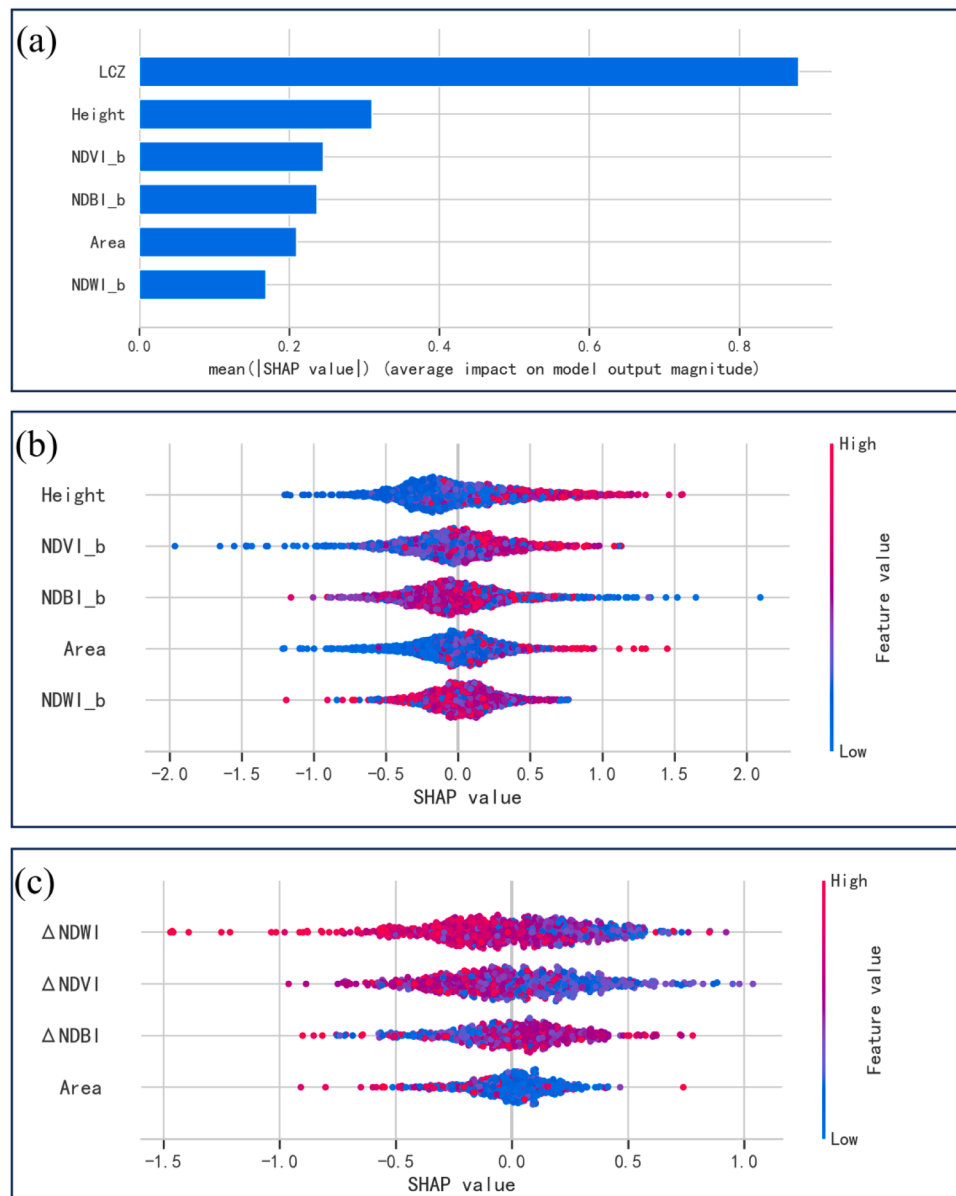


Fig. 9. Determinants of green roof cooling efficacy. (a) SHAP feature importance measured as the mean absolute Shapley values and (b) SHAP summary plot showing the influences of different factor on green roof cooling efficacy based on type II green roofs in 2024, and (c) SHAP summary plot showing the importance and detailed performance of different factors influencing green roof cooling efficacy based on type I green roofs.

of Type II green roofs relative to their surrounding bare roofs during the summer of 2024. Comparative analysis revealed that Type II green roofs demonstrated consistently lower mean LST values relative to the surrounding bare roofs within the 500-m buffer zone (Fig. 8). Quantitative evaluation showed 76.62 % of Type II green roofs maintained reduced LST values compared to surrounding bare roofs, while 23.38 % exhibited elevated LST readings. Specifically, the average surface temperature of Type II green roofs was 36.61 °C, while the average temperature of surrounding bare roofs was 39.10 °C, resulting in a temperature reduction 2.49 °C attributable to green roof implementation.

Further analysis revealed that 76.62 % of Type II green roofs exhibited measurable thermal mitigation, with varying degrees of cooling efficacy. Notably, 26.77 % of these roofs achieved a temperature reduction of more than 3 °C, highlighting their significant cooling potential.

3.2.3. Determinants of green roof's cooling efficacy

The study employed a machine learning-based approach to identify

the key determinants governing the cooling efficacy of green roofs. The RF model revealed that LCZ was the dominant predictor, with substantially higher feature importance compared to other variables (Fig. 9a). The finding underscores the pivotal role of urban morphology and surface cover in determining the green roof cooling performance. Following LCZ, building height emerged as the second most important factor, suggesting that taller buildings may experience different cooling effects due to variations in wind patterns, solar exposure, or heat distribution. Surrounding green vegetation cover, as indicated by NDVI, ranked third in importance, emphasizing the contribution of nearby greenery in enhancing the cooling effect. Other factors, such as built environment intensity (NDBI), green roof area (Area), and blue infrastructure (NDWI) also played significant roles but to a lesser extent compared to LCZ and building height.

SHAP further quantifies directionality and interactions among continuous predictors (Fig. 9b). A higher building height and surrounding vegetation cover enhances cooling. Similarly, a bigger green roof present greater thermal mitigation capacity. However, higher

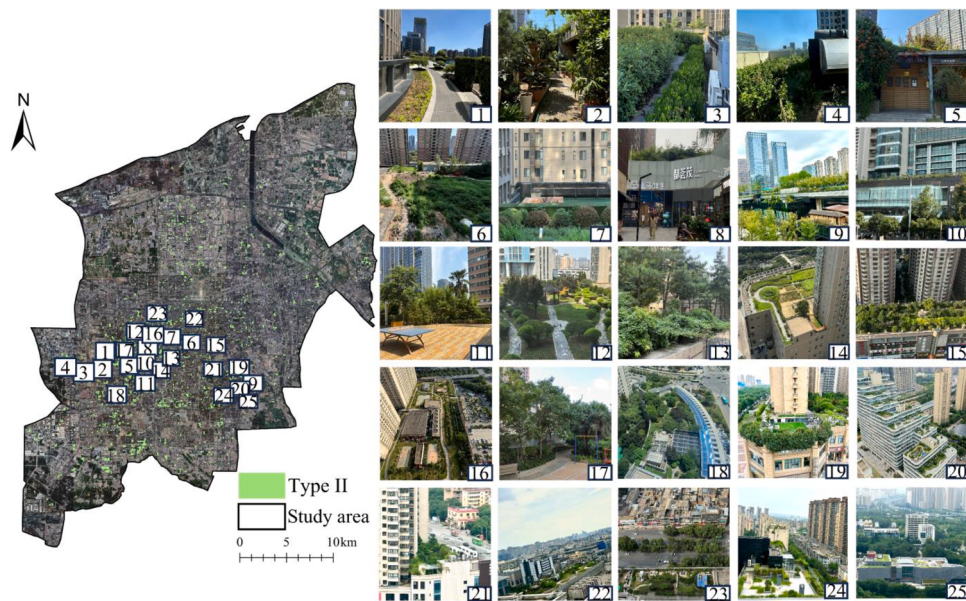


Fig. 10. The distribution of 25 type II green roofs selected for field investigation. (1)-(25) are the photos taken on site.

surrounding built environment intensity tends to weaken green roofs' cooling efficacy.

The analysis further revealed that environmental changes, such as the expansion of blue infrastructure and improved vegetation cover within a 500-meter buffer zone, positively correlated with enhanced green roof cooling efficiency (Fig. 9c). Conversely, increased building density in adjacent areas exhibited a weakening effect on thermal regulation performance.

3.2.4. Field investigation results

To validate the cooling effects observed through remote sensing analysis, a field investigation was conducted on a sample of 25 Type II green roofs during the summer of 2024. Fig. 10 and Table 3 revealed distinct microclimatic disparities between vegetated and non-vegetated roof systems, confirming the effectiveness of green roofs in reducing temperature and increasing humidity. Specifically, the average surface temperature of green roofs was found to be 4.83 °C (31.78 °C vs. 36.61 °C) lower than that of surrounding bare roofs, while the air humidity in green roof areas was 26.40 % (37.88 % vs. 11.48 %) higher. These findings not only corroborate the remote sensing data but also highlight the dual benefits of green roofs in mitigating heat and retaining moisture.

In addition, the field investigation revealed variations in the cooling and moisture regulation performance of different green roof types. The intensive garden configuration having a 9.45 % higher moisture regulation performance and a 2.26 °C lower temperature regulation performance than the semi-intensive and extensive configurations. For example, the ID2 case study illustrated vertical architectural compensation through biodiverse design integration despite its elevated vertical profile, the system achieved optimized cooling-humidification synergy via multi-phytocoenosis composition and aquatic microenvironment integration. This observation underscores the importance of green roof design in optimizing both cooling and humidity regulation performance.

4. Discussion

4.1. Cooling effects of green roofs: mechanisms and regional variations

Our multi-dimensional analysis of green roof performance in Xi'an, a representative northwestern Chinese metropolis, reveals three critical findings about urban-scale thermal mitigation. First, the 2019–2022

green roof expansion (0.28 km²) in Xi'an's urban core yielded a measurable 0.47 °C temperature reduction, demonstrating consistent efficacy across climate regions. This aligns with Dong et al.'s (2020) observation of 0.91 °C cooling in subtropical Xiamen and Jin et al. (2022) documentation of 0.5 °C reduction in temperate Chengdu, establishing a robust cross-climate validation of green roof effectiveness. Moreover, regional climate also modulates the cooling mechanisms. While southern Chinese cities benefit from enhanced evaporative cooling in humid conditions (0.91 °C reduction), our data show drought-adapted species in Xi'an's arid summer climate still achieve significant though attenuated cooling (0.47 °C). This differential performance underscores the need for climate-specific vegetation selection in green roof design.

Second, our LCZ-based analysis extends previous findings (Jin et al., 2022; Jia et al., 2025) by identifying optimal green roof implementation zones. The strongest thermal mitigation occurs in compact high-rise areas (LCZ 1), where microclimate challenges are most acute. Furthermore, we establish that environmental context - particularly vegetation cover, built environment intensity and blue infrastructure - mediates green roof performance through evapotranspiration capacity, shading efficiency and local heat island intensity. Current limitations in spatial autocorrelation handling and seasonal analysis suggest the methodological improvements for future research including multi-temporal remote sensing integration and expanded buffer zone analysis.

Third, the observed performance variations among green roof types highlight an important design consideration. As demonstrated by Lazarin et al. (2005) and later studies (Jamei et al., 2023; Zhang et al., 2020), multi-layered "tree-shrub-herb" systems achieve superior cooling through combined evapotranspiration and shading effects. This finding directly informs sustainable urban planning by emphasizing vegetation configuration as a critical performance determinant.

4.2. Implications for future study

Our 2024 assessment revealed that existing green roofs (covering 1.41 km², representing 1.78 % of total roof area in the study region) demonstrated significant urban cooling effects, with an average temperature reduction of 2.49 °C across the study area. Given Xi'an's current limited green roof coverage (substantially below the 20–30 % greenery coverage benchmark recommended by Ng et al. (2012) for sustainable urban design), our findings suggest considerable untapped potential for thermal mitigation through strategic expansion of roof

Table 3
Field investigation results.

ID	Locations	Floor of the building	Types of green roof	Measure time	Wind Direction/Speed	Green roofs		Surrounding bare roofs	
						Humidity/%	Air temperature/ °C	Humidity/%	Air temperature/ °C
1	The Orange Crystal Hotel	7F	Garden style	12:00	Northeast wind/0.5m/s	32 %	31.5	4 %	37.5
2	Zhongqing Building	26F	Garden style	13:00	Northeast wind/0.8m/s	42 %	31.8	12 %	37.2
3	Xinghe Jiayuan Community	3F	Semi-garden style	15:00	Northeast wind/1.5m/s	44 %	33.3	8 %	36.4
4	Tiandiyan Yunshui Tianjing Community	3F	Simplex	15:30	Northeast wind/1.4m/s	28 %	33.8	10 %	35.8
5	Public Toilet	1F	Simplex	13:30	Northeast wind/1.7m/s	33 %	33.4	15 %	36.6
6	Western Gold and Jewelry Mall	5F	Semi-garden style	14:30	Northeast wind/3.1m/s	28 %	32.3	9 %	36.7
7	Zhongmao Mall	5F	Garden style	15:00	Northeast wind/3m/s	41 %	31.5	11 %	35.9
8	Gaoxin Daduhui Mall	1F	Garden style	14:30	Northeast wind 2m/s	38 %	30.5	12 %	37.1
9	Qujiang Creative Circle Mall	3F	Garden style	15:00	Northeast wind/1.8m/s	48 %	30.7	6 %	36.9
10	EYANG Guoji Building	4F	Semi-garden style	14:40	Northeast wind/2m/s	33 %	32.5	14 %	37.5
11	Yamei Buliding	3F	Garden style	11:00	Northeast wind/1.2m/s	50 %	30.1	18 %	35.8
012	Park Capital Yijing Guoji	4F	Garden style	12:00	Northeast wind/1.7m/s	43 %	31.5	7 %	36.3
13	Eaton House Community	1F	Garden style	12:30	Northeast wind/2m/s	39 %	30.4	12 %	36.8
14	Ruixin Motiancheng Apartment	5F	Garden style	13:30	Northeast wind/1.8m/s	35 %	30.6	9 %	37.2
15	Xi Hehua Yuan Community	5F	Garden style	15:30	Northeast wind/1.8m/s	52 %	30.2	18 %	35.2
16	Shengshi Square Taibai Community	6F	Garden style	15:40	Northeast wind/2.7m/s	46 %	29.9	17 %	35.5
17	Wutong Langzuo Apartment	5F	Garden style	15:00	Northeast wind/2.1m/s	48 %	29.4	10 %	36.1
18	Shanxi Investment Building	4F	Garden style	14:00	Northeast wind/1.7m/s	39 %	31.5	11 %	37.7
19	Hezhong Qujiang City Community	2F	Semi-garden style	12:20	Northeast wind/2m/s	31 %	32.8	12 %	37.2
20	Qujiang Babylon Art Garden Apartment	22F	Garden style	13:00	Northeast wind/2.3m/s	26 %	33.1	12 %	36.4
21	Qijulin Company	3F	Simplex	13:30	Northeast wind/1.9m/s	22 %	34.9	13 %	36.8
22	Qunguang Mall	7F	Semi-garden style	14:30	Northeast wind/2.1m/s	33 %	32.3	13 %	36.3
23	Kaiyuan Mall Xiwang shopping Mall	6F	Garden style	15:00	Northeast wind/2m/s	38 %	30.4	13 %	35.9
24	Qujiang Rose Garden community	18F	Garden style	14:00	Northeast wind/1.8m/s	32 %	32.4	13 %	36.8
25	Xi'an Comprehensive Disaster Reduction Science Museum	4F	Simplex	13:40	Northeast wind/2.4m/s	28 %	33.8	8 %	37.6

greening systems.

The optimal implementation of new green roofs requires careful consideration of multiple factors: (1) localized cooling capacity variations across different LCZs, (2) site-specific environmental conditions, (3) structural suitability of individual roofs, and (4) equitable spatial distribution across urban sectors. To inform future urban planning, we propose a comprehensive simulation framework evaluating cooling effects under varying coverage scenarios and spatial configurations. This simulation approach incorporates three key methodological innovations:

- (1) Deep learning or even artificial intelligence methods for automated identification of structurally suitable roofs;
- (2) Multi-criteria allocation modeling of green roof area in different urban parts that balances cooling efficiency (by LCZ) with spatial equity considerations;

(3) Stratified random sampling within each LCZ with environmental parameter-based adjustments.

The proposed methodology provides urban planners with a scientifically-grounded, data-driven approach to maximize the thermal benefits of green roof implementation while addressing practical constraints and social equity concerns.

4.3. Implementation challenges and sustainable trade-offs in green roof deployment

While our findings substantiate the thermal mitigation benefits of green roofs in Xi'an's urban environment and reveal substantial expansion potential, their widespread implementation presents complex sustainability trade-offs that warrant careful consideration. In semi-arid urban ecosystems exemplified by Xi'an, drought-resilient vegetation systems require precisely calibrated irrigation protocols during

extended dry periods, as elevated evapotranspiration rates coupled with precipitation deficits induce acute hydrological strain. Overreliance on municipal water supplies could exacerbate urban water scarcity, necessitating the integration of rainwater harvesting systems or reclaimed water reuse technologies to mitigate dependency.

Furthermore, operational challenges persist in lifecycle maintenance frameworks. Inadequate long-term maintenance of green roofs may lead to vegetation mortality, compromising their aesthetic appeal and functional performance. Exposed substrate during heavy rainfall events can intensify soil erosion. It is imperative to establish monitoring mechanisms, incorporate green roofs into urban resilience planning frameworks, and synergistically optimize their integration with gray infrastructure (e.g., drainage networks) to ensure systemic functionality.

5. Conclusions

This study systematically examined the cooling effects of green roofs in the urban core of Xi'an, China, using multi-source remote sensing data and GIS technology. Our objectives were to: (1) assess the cooling effect of green roofs through inter-year comparisons of roofs before and after greening; (2) evaluate the magnitude of cooling effects by comparing green roofs with surrounding bare roofs within the same year; and (3) identify the key determinants influencing green roof cooling efficacy using machine learning approaches.

Our findings provide a clear demonstration of the significant cooling effects of green roofs at both the urban and local scales. Specifically, Type I green roofs (those not green in 2019 but green in 2022) contributed to a temperature reduction of 0.47 °C across the study area. Furthermore, an intra-year comparison revealed that Type II green roofs (all green roofs in 2024) showed an average temperature decrease of 2.49 °C compared to surrounding bare roofs. These results underscore the efficacy of green roofs in mitigating urban heat island effects.

A prime contribution of this investigation is the identification of Local Climate Zone (LCZ) as the dominant predictor of green roof cooling efficacy. Our analysis highlights that the microclimate characteristics defined by LCZ, such as urban morphology and surface cover, play a pivotal role in determining the cooling performance of green roofs. Additionally, we found that concurrent enhancements in surrounding blue infrastructure and vegetation amplify the cooling performance, while increased built-up density exhibits thermal interference. These findings provide valuable insights into the context-dependent optimization strategies for urban heat mitigation.

In conclusion, this study underscores the significant potential of green roofs in reducing urban temperatures and contributing to a more sustainable urban environment. Our findings emphasize the importance of comprehensive planning that considers the relationship between green roof design and the surrounding landscape and building environment. These results can inform urban planners and policymakers in developing strategic green infrastructure to enhance the resilience and sustainability of cities.

CRediT authorship contribution statement

Xiya Yan: Writing – original draft, Methodology, Investigation, Formal analysis, Data curation. **Jianhong Liu:** Writing – review & editing, Supervision, Methodology, Funding acquisition, Formal analysis. **Wei Zhang:** Data curation. **Ziqi Wang:** Investigation, Data curation. **Ruolan Jia:** Formal analysis. **Lei Wang:** Data curation. **Nan Liu:** Investigation. **Yu Zhu:** Formal analysis.

Declaration of competing interest

The authors declare that they have no known competing financial interests or personal relationships that could have appeared to influence the work reported in this paper.

Acknowledgments

This research was funded by the Natural Science Foundation of Shaanxi Province (NO. 2023-JC-YB-253).

Supplementary materials

Supplementary material associated with this article can be found, in the online version, at doi:[10.1016/j.scs.2025.106545](https://doi.org/10.1016/j.scs.2025.106545).

Data availability

The authors do not have permission to share data.

Reference

- Barsi, J. A., Schott, J. R., Palluconi, F. D., et al. (2005). Validation of a web-based atmospheric correction tool for single thermal band instruments. In , 58820. *Proceedings of SPIE - The International Society for Optical Engineering*. <https://doi.org/10.1117/12.619990>
- Berardi, U. (2016). The outdoor microclimate benefits and energy saving resulting from green roofs retrofits. *Energy and Buildings*, 121, 217–229. <https://doi.org/10.1016/j.enbuild>, 2016.03.021.
- Breiman, L. (2001). Random forests. *Machine Learning*, 45, 5–32. <https://doi.org/10.1023/A:1010933404324>
- Bonafoni, S., Annibale, R., & Pierdicca, N. (2015). Downscaling of the land surface temperature over urban areas using landsat data. In *2015 IEEE International Geoscience and Remote Sensing Symposium (IGARSS)* (pp. 1144–1147). <https://doi.org/10.1109/IGARSS.2015.7325973>
- Chaves, M. E. D., Picoli, M. C. A., & Sanches, I. D. (2020). Recent applications of Landsat 8/OLI and Sentinel-2/MSI for land use and land cover mapping: A systematic review. *Remote Sensing*, 12(18), 3062. <https://doi.org/10.3390/rs12183062>
- China Statistical Yearbook. China Statistics Press. (2018). [in Chinese].
- Cichowicz, R., & Bochenek, A. D. (2024). Assessing the effects of urban heat islands and air pollution on human quality of life. *Anthropocene*, , Article 100433. <https://doi.org/10.1016/j.anocene.2024.100433>
- Degefu, M. A., Argaw, M., Feyisa, G., et al. (2023). Dynamics of green spaces- land surface temperature intensity nexus in cities of Ethiopia. *Heliyon*, 9, Article e13274. <https://doi.org/10.1016/j.heliyon.2023.e13274>
- Devadas, M. D., & Rose, A. L. (2009). Urban factors and the intensity of heat island in the city of Chennai. In *The seventh International Conference on Urban Climat*.
- Dominguez, A., Kleissl, J., Luval, J. C., et al. (2011). High-resolution urban thermal sharpener (HUTS). *Remote Sensing of Environment*, 115(7), 1772–1780. <https://doi.org/10.1016/j.rse.2011.03.008>
- Dong, J., Lin, M. X., Jin, Z., et al. (2020). Quantitative study on the cooling effect of green roofs in a high-density urban area—A case study of Xiamen, China. *Journal of Cleaner Production*, 255, Article 120152. <https://doi.org/10.1016/j.jclepro.2020.120152>
- Gao, S. J., Chen, Y. H., Chen, D. L., et al. (2024). Urbanization-induced warming amplifies population exposure to compound heatwaves but narrows exposure inequality between global North and South cities. *npj Climate and Atmospheric Science*, 7, 154. <https://doi.org/10.1038/s41612-024-00708-z>
- Georgescu, M., Mousaoui, M., Mahalov, A., et al. (2013). Summer-time climate impacts of projected megapolitan expansion in Arizona. *Nature Climate Change*, 3, 37–41. <https://doi.org/10.1038/NCLIMATE1656>
- Guan, Z. C. (2019). *Research on green roof practice and landscape evaluation in Xi'an city*. Northwest A&F University. Master's thesisMaster's degree(in Chinese with English abstract).
- Herrera-Gomez, S., Quevedo-Nolasco, A., & Pérez-Urrestarazu, L. (2017). The role of green roofs in climate change mitigation. A case study in Seville (Spain). *Building and Environment*, 123, 575–584. <https://doi.org/10.1016/j.buildenv.2017.07.036>
- Gunawardena, K. R., Wells, M. J., & Kershaw, T. (2017). Utilising green and bluespace to mitigate urban heat island intensity. *Science of the total environment*, 584, 1040–1055. <https://doi.org/10.1016/j.scitotenv.2017.01.158>
- He, Y., Yu, H., Ozaki, A., et al. (2020). Thermal and energy performance of green roof and cool roof: A comparison study in Shanghai area. *Journal of Cleaner Production*, 267, Article 122205. <https://doi.org/10.1016/j.jclepro.2020.122205>
- Huete, A., Didan, K., Miura, T., et al. (2002). Overview of the radiometric and biophysical performance of the MODIS vegetation indices. *Remote Sensing of Environment*, 83, 195–213. [https://doi.org/10.1016/S0034-4257\(02\)00096-2](https://doi.org/10.1016/S0034-4257(02)00096-2)
- Imran, H. M., Kala, J., Ng, A. W. M., et al. (2018). Effectiveness of green and cool roofs in mitigating urban heat island effects during a heatwave event in the city of Melbourne in southeast Australia. *Journal of Cleaner Production*, 197, 393–405. <https://doi.org/10.1016/j.jclepro.2018.06.179>
- Jahangir, M. H., Zarfeshani, A., & Arast, M. (2024). Investigation of green roofs effects on reducing of the urban heat islands formation (The case of a municipal district of Tehran City, Iran). *Nature-Based Solutions*, 5, Article 100100. <https://doi.org/10.1016/j.nbsj.2023.100100>
- Jamei, E., Thirunavukkarasu, G., Chau, H. W., et al. (2023). Investigating the cooling effect of a green roof in Melbourne. *Building and Environment*, 246, Article 110965. <https://doi.org/10.1016/j.buildenv.2023.110965>

- Jia, S. Q., Weng, Q. H., Yoo, C., et al. (2025). Global investigation of pedestrian-level cooling and energy-saving potentials of green and cool roofs in 43 megacities. *Energy & Buildings*, 337. <https://doi.org/10.1016/j.enbuild.2025.115671>
- Jin, Z., Ma, J. H., Lin, T., et al. (2022). Quantitative valuation of green roofs' cooling effects under different urban spatial forms in high-density urban area. *Building and Environment*, 222, Article 109367. <https://doi.org/10.1016/j.buildenv.2022.109367>
- Kafy, A. A., Crews, K. A., & Thompson, A. E. (2024). Exploring the cooling potential of green roofs for mitigating diurnal heat island intensity by utilizing lidar and artificial neural network. *Sustainable Cities and Society*, 116, 18. <https://doi.org/10.1016/j.scs.2024.105893>
- Katarina, O., Michal, G., Daniel, P., et al. (2022). Combining Landsat 8 and Sentinel-2 data in Google Earth engine to derive higher resolution land surface temperature maps in urban environment. *Remote Sensing*, 14, 4076. <https://doi.org/10.3390/rs1464076>
- Keramitsoglou, I., Kiranoudis, C. T., & Weng, Q. (2013). Downscaling geostationary land surface temperature imagery for urban analysis. *IEEE Geoscience and Remote Sensing Letters*, 10(5), 1253–1257. <https://doi.org/10.1109/LGRS.2013.2257668>
- Kim, J. H., Choi, S., Panahi, M., et al. (2025). Deep learning-based spatial optimization of green and cool roof implementation for urban heat mitigation. *Journal of Environmental Management*, 383, Article 125398. <https://doi.org/10.1016/j.jenvman.2025.125398>
- Kroeger, C., & Koustava, S. (2023). Heat is associated with short-term increases in household food insecurity in 150 countries and this is mediated by income. *Nature Human Behaviour*, 7, 1777–1786. <https://doi.org/10.1038/s41562-023-01684-9>
- Kumar, V. V., & Mahalle, A. M. (2016). Green roofs for energy conservation and sustainable development: A review. *International Journal of Applied Engineering Research*, (11–4 Pt.7).
- Kustas, W. P., Norman, J. M., Anderson, M. C., et al. (2003). Estimating subpixel surface temperatures and energy fluxes from the vegetation index-radiometric temperature relationship. *Remote Sensing of Environment*, 85(4), 429–440. [https://doi.org/10.1016/S0034-4257\(03\)00036-1](https://doi.org/10.1016/S0034-4257(03)00036-1)
- Lazzarin, R. M., Castellotti, F., & Busato, F. (2005). Experimental measurements and numerical modelling of a green roof. *Energy & Buildings*, 37(12), 1260–1267. <https://doi.org/10.1016/j.enbuild.2005.02.001>
- Liang, F., Liu, J. H., Liu, M. X., et al. (2021). Scale-dependent impacts of urban morphology on commercial distribution: A case study of Xi'an, China. *Land*, 10, 170. <https://doi.org/10.3390/land10020170>
- Liu, M. X., Dong, J., Jones, L., et al. (2021). Modeling green roofs' cooling effect in high-density urban areas based on law of diminishing marginal utility of the cooling efficiency: A case study of Xiamen island, China. *Journal of Cleaner Production*, 316, Article 128277. <https://doi.org/10.1016/j.jclepro.2021.128277>
- Liu, H. P., Zhu, Y. Z., Dai, P. L., et al. (2009). Analysis of urban climate characteristics in Zhengzhou. *Meteorological and Environmental Science*, 32(1), 72–74 [in Chinese].
- Liu, M. X., Ma, M. F., Liu, J. H., et al. (2023). Quantifying impacts of natural and anthropogenic factors on urban ecological quality changes: A multiscale survey in Xi'an, China. *Ecological Indicators*, 153, Article 110463. <https://doi.org/10.1016/j.ecolind.2023.110463>
- Liu, M. X., Liu, J. H., Atzberger, C., et al. (2021). Zanthoxylum bungeanum maxim mapping with multi-temporal Sentinel-2 images: The importance of different features and consistency of results. *ISPRS Journal of Photogrammetry and Remote Sensing*, 174, 68–86. <https://doi.org/10.1016/j.isprsjprs.2021.02.003>
- Liu, Z. H., Zhan, W. F., Bechtel, B., et al. (2022). Surface warming in global cities is substantially more rapid than in rural background areas. *Communications Earth & Environment*, 3, 219. <https://doi.org/10.1038/s43247-022-00539-x>
- Li, J. N., Liu, J. H., Liu, M. X., et al. (2023). Urban ecological environment evaluation and influencing factors analysis at the residential quarter-level in Xi'an, China. *Ecological Indicators*, 158, Article 111348. <https://doi.org/10.1016/j.ecolind.2023.111348>
- Li, D., Bou-Zeid, E., & Oppenheimer, M. (2014). The effectiveness of cool and green roofs as urban heat island mitigation strategies. *Environmental Research Letters*, (5), Article 055002. <https://doi.org/10.1088/1748-9326/9/5/055002>
- Liu, Z. Y., & Zhang, S. S. (2025). Exploring the relationship between urban green development and heat island effect within the Yangtze River Delta Urban Agglomeration. *Sustainable Cities and Society*, 121, Article 106204. <https://doi.org/10.1016/j.scs.2025.106204>
- Lundberg, S. M., & Lee, S. I. (2017). A unified approach to interpreting model predictions. *Neural Information Processing Systems*, 30. <https://doi.org/10.48550/arXiv.1705.07874>
- Ng, E., Chen, L., Wang, Y. N., et al. (2012). A study on the cooling effects of greening in a high-density city: An experience from Hong Kong. *Building and Environment*, 47(1), 256–271. <https://doi.org/10.1016/j.buildenv.2011.07.014>
- Nirwana, H. D., Saidy, A. R., Hatta, G. M., et al. (2024). Design of a green city with lower carbon based on vegetation in Banjarbaru using Sentinel-2. *Journal of Agricultural and Development Sciences*, 5(2). <https://doi.org/10.47738/jads.v5i2.218>
- Pettorelli, N., Vik, J. O., Mysterud, A., et al. (2005). Using the satellite-derived NDVI to assess ecological responses to environmental change. *Trends in Ecology & Evolution*, 20, 503–510. <https://doi.org/10.1016/j.tree.2005.05.011>
- Phelan, P. E., Kaloush, K., Miner, M., et al. (2015). Urban heat island: Mechanisms, implications, and possible remedies. *Annual Review of Environment & Resources*, 40, 285–307. <https://doi.org/10.1146/annurev-environ-102014-021155>
- Qu, L. W., Xu, J. J., Zhu, Q. L., et al. (2018). Atmospheric circulation anomalies and causes of the 2017 high temperature event in Shaanxi. *Shaanxi Meteorology*, (5), 4 [In Chinese with English abstract].
- Reed, B. C., Brown, J. F., Thomas, R. D. V., et al. (1994). Measuring phenological variability from satellite imagery. *Journal of Vegetation Science*, 5, 703–714. <https://doi.org/10.2307/3235884>
- Sailor, D. J. (2014). A holistic view of the effects of urban heat island mitigation. *Environmental Science, Engineering*. <https://doi.org/10.1016/j.scientificdirect.2014.09.001>
- Schmitz, H. J., Jauch, M., Krummradt, I., et al. (2018). Increasing evapotranspiration of extensive roof greenings by using plants with high transpiration rates and irrigation with grey water. *Acta Horticultae*, 1215, 53–56. <https://doi.org/10.17660/ActaHortic.2018.1215.9>
- Sharma, A., Conry, P., Fernando, H. J. S., et al. (2016). Green and cool roofs to mitigate urban heat island effects in the Chicago metropolitan area: Evaluation with a regional climate model. *Environmental Research Letters*, 11(6), Article 064004. <https://doi.org/10.1088/1748-9326/11/6/064004>
- Srivastava, S., & Ahmed, T. (2022). Correlation between built-up and land surface temperature using Sentinel-2 and Landsat-8 images through semi-supervised deep learning model for efficient land surface monitoring. *Mathematical Statistician and Engineering Applications*, 71(4), 3000–3023. <https://doi.org/10.17762/msea.v7i4.859>
- Tan, H. C., Kotamarthi, R., Wang, J. L., et al. (2022). Impact of different roofing mitigation strategies on near-surface temperature and energy consumption over the Chicago metropolitan area during a heatwave event. *Science of the Total Environment*, 860, 160508. <https://doi.org/10.1016/j.scitotenv.2022.160508>
- Tan, X. Y., Sun, X., Huang, C. D., et al. (2021). Comparison of cooling effect between green space and water body. *Sustainable Cities and Society*, 67, Article 102711. <https://doi.org/10.1016/j.scs.2021.102711>
- Wang, C. H., Song, J. Y., Shi, D. C., et al. (2023). Impacts of climate change, population growth, and power sector decarbonization on urban building energy use. *Nature Communications*, 14, 6434. <https://doi.org/10.1038/s41467-023-41458-5>
- Wang, Q., Wang, X. N., Zhou, Y., et al. (2022). The dominant factors and influence of urban characteristics on land surface temperature using random forest algorithm. *Sustainable Cities and Society*, 79, Article 103722. <https://doi.org/10.1016/j.scs.2022.103722>
- Wang, S. S., Zhan, W. F., Zhou, B. B., et al. (2025). Dual impact of global urban overheating on mortality. *Nature Climate Change*, 15, 497–504. <https://doi.org/10.1038/s41558-025-02303-3>
- Wang, X., Li, H. D., & Sodoudi, S. (2022). The effectiveness of cool and green roofs in mitigating urban heat island and improving human thermal comfort. *Building and Environment*, 217. <https://doi.org/10.1016/j.buildenv.2022.109082>
- Xi'an Statistical Yearbook. (2023). [in Chinese].
- Yang, Q. Q., Huang, X., & Tang, Q. H. (2019). The footprint of urban heat island effect in 302 Chinese cities: Temporal trends and associated factors. *The Science of the Total Environment*, 655, 652–662. <https://doi.org/10.1016/j.scitotenv.2018.11.171>
- Zhang, H., Kang, M. Y., Guan, Z. R., et al. (2024). Assessing the role of urban green infrastructure in mitigating summertime urban heat island (UHI) effect in metropolitan Shanghai, China. *Sustainable Cities and Society*, 112, Article 105605. <https://doi.org/10.1016/j.scs.2024.105605>
- Zhang, G. C., He, B. J., & Dewancker, B. J. (2020). The maintenance of prefabricated green roofs for preserving cooling performance: A field measurement in the subtropical city of Hangzhou, China. *Sustainable Cities and Society*, 61, Article 102314. <https://doi.org/10.1016/j.scs.2020.102314>
- Zhang, Y. Z., Wu, P. H., Duan, S. B., et al. (2021). Downscaling of Landsat 8 land surface temperature products based on deep learning. *National Remote Sensing Bulletin*, 08–1767-11 [in Chinese with English abstract].
- Zheng, X. D., Kong, F. H., Yin, H. W., et al. (2021). Outdoor thermal performance of green roofs across multiple time scales: a case study in subtropical China. *Sustainable Cities and Society*, 70(2), 102909. <https://doi.org/10.1016/j.scs.2021.102909>
- Zheng, Y., Keeffe, G., & Mariotti, J. (2023). Nature-based solutions for cooling in high-density neighbourhoods in Shenzhen: A case study of Baishizhou. *Sustainability*, 15 (6). <https://doi.org/10.3390/su15065509> (2071-1050).
- Zhou, B. H., Liu, Z. H., & Dong, Y. (2017). Atmospheric temperature variation and its causes in summer of Jinan for 2015. In *2017 7th International Conference on Education, Management, Computer and Society (EMCS 2017)* (pp. 1464–1471). Atlantis Press.
- Zhu, J. H., Zhu, S. Y., Yu, F. C., et al. (2021). A downscaling method for ERA5 reanalysis land surface temperature over urban and mountain areas. *National Remote Sensing Bulletin*, 25(08) [in Chinese with English abstract].
- Zhuang, Q. R., & Lu, Z. M. (2021). Optimization of roof greening spatial planning to cool down the summer of the city. *Sustainable Cities and Society*, 74, Article 103221. <https://doi.org/10.1016/j.scs.2021.103221>
- Yuan, B., Zhou, L., Hu, F. N., et al. (2022). Diurnal dynamics of heat exposure in Xi'an: A perspective from local climate zone. *Building and Environment*, 222. <https://doi.org/10.1016/j.buildenv.2022.109400>